

### RESEARCH ARTICLE

10.1002/2014WR015335

#### Key Points:

- We study experimentally the impact of capillarity on a buoyant gravity current
- We show that capillary pressure hysteresis can stop migration of the current
- Capillary pinning can be an effective trapping mechanism in CO<sub>2</sub> sequestration

#### Supporting Information:

- Readme
- Video of micromodel simulation
- Video of micromodel experiment

#### Correspondence to:

R. Juanes,  
juanes@mit.edu

#### Citation:

Zhao, B., C. W. MacMinn, H. E. Huppert, and R. Juanes (2014), Capillary pinning and blunting of immiscible gravity currents in porous media, *Water Resour. Res.*, 50, 7067–7081, doi:10.1002/2014WR015335.

Received 22 JAN 2014

Accepted 1 AUG 2014

Accepted article online 5 AUG 2014

Published online 3 SEP 2014

## Capillary pinning and blunting of immiscible gravity currents in porous media

Benzhong Zhao<sup>1</sup>, Christopher W. MacMinn<sup>2</sup>, Herbert E. Huppert<sup>3,4,5</sup>, and Ruben Juanes<sup>1</sup>

<sup>1</sup>Department of Civil and Environmental Engineering, Massachusetts Institute of Technology, Cambridge, Massachusetts, USA, <sup>2</sup>Department of Engineering Science, University of Oxford, Oxford, UK, <sup>3</sup>Department of Applied Mathematics and Theoretical Physics, Institute of Theoretical Geophysics, University of Cambridge, Cambridge, UK, <sup>4</sup>School of Mathematics, University of New South Wales, Kensington, New South Wales, Australia, <sup>5</sup>Faculty of Science, University of Bristol, Bristol, UK

**Abstract** Gravity-driven flows in the subsurface have attracted recent interest in the context of geological carbon dioxide (CO<sub>2</sub>) storage, where supercritical CO<sub>2</sub> is captured from the flue gas of power plants and injected underground into deep saline aquifers. After injection, the CO<sub>2</sub> will spread and migrate as a buoyant gravity current relative to the denser, ambient brine. Although the CO<sub>2</sub> and the brine are immiscible, the impact of capillarity on CO<sub>2</sub> spreading and migration is poorly understood. We previously studied the early time evolution of an immiscible gravity current, showing that capillary pressure hysteresis pins a portion of the macroscopic fluid-fluid interface and that this can eventually stop the flow. Here we study the full lifetime of such a gravity current. Using tabletop experiments in packings of glass beads, we show that the horizontal extent of the pinned region grows with time and that this is ultimately responsible for limiting the migration of the current to a finite distance. We also find that capillarity blunts the leading edge of the current, which contributes to further limiting the migration distance. Using experiments in etched micromodels, we show that the thickness of the blunted nose is controlled by the distribution of pore-throat sizes and the strength of capillarity relative to buoyancy. We develop a theoretical model that captures the evolution of immiscible gravity currents and predicts the maximum migration distance. By applying this model to representative aquifers, we show that capillary pinning and blunting can exert an important control on gravity currents in the context of geological CO<sub>2</sub> storage.

### 1. Introduction

Gravity currents refer to the predominantly horizontal gravity-driven flow of two fluids with different densities. Gravity currents are prevalent in nature and they occur in the atmosphere, the ocean, and the subsurface [Huppert, 2006]. Gravity currents in porous media have been well studied in the past in the context of miscible fluids [Barenblatt, 1952; Bear, 1972; Huppert and Woods, 1995]. Results from these studies have become important predictors for a wide range of processes such as seawater intrusions into freshwater aquifers [Lee and Cheng, 1974; Frind, 1982] and drilling-fluid migration into surrounding reservoirs [Dussan and Auzeais, 1993]. More recently, the study of gravity currents in porous media has provided new insights into the storage of carbon dioxide (CO<sub>2</sub>) in deep geological reservoirs such as saline aquifers [Nordbotten et al., 2006; Bickle et al., 2007; Hesse et al., 2007; Juanes et al., 2010; MacMinn et al., 2011]. Because CO<sub>2</sub> is less dense than the ambient brine in those reservoirs, the CO<sub>2</sub> will migrate upward due to buoyancy and spread along the top boundary of the aquifer as a gravity current.

While capillarity is absent in miscible gravity currents, it plays an important role in gravity currents with immiscible fluids. Immiscible gravity currents are relevant in processes such as the migration of dense nonaqueous phase liquid (DNAPL) contamination in groundwater aquifers [Illangasekare et al., 1995; Pennell et al., 1996; Ewing and Berkowitz, 2001], as well as CO<sub>2</sub> storage in deep saline aquifers [Hesse et al., 2008; MacMinn et al., 2010, 2011; Gasda et al., 2011]. A well-studied effect of capillarity in immiscible gravity currents is residual trapping, where tiny blobs of nonwetting fluid become surrounded by wetting fluid and become immobilized in the pore space [Juanes et al., 2006; Hesse et al., 2008; Juanes et al., 2010; MacMinn et al., 2010]. In addition to residual trapping, capillary forces create a partially saturated layer between the

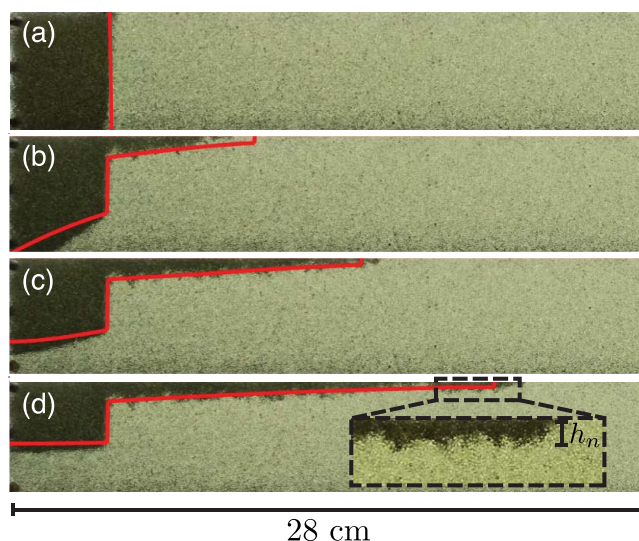


**Figure 1.** Gravity-driven flow of a buoyant, nonwetting fluid (air) over a dense, wetting fluid (propylene glycol) in a packing of glass beads. (a and b) Starting with a vertical interface between the fluids, the flow first undergoes a lock-exchange process. (c and d) The process models a finite-release problem after the dense fluid reaches the left boundary. In contrast to the finite release of a miscible current that spreads indefinitely, spreading of an immiscible current stops at a finite distance. Dashed black box highlights the blunt nose of the current, which has thickness  $h_n$  (see section 3.2). Red lines represent predictions from our macroscopic sharp-interface model (see section 4).

*et al.* [2013] described the early time evolution of immiscible gravity currents (i.e., exchange flow), the late-time behavior of immiscible gravity currents has not been studied experimentally.

Here, we study the entire evolution of immiscible gravity currents via release of a finite volume of buoyant nonwetting fluid into a dense wetting fluid in a vertically confined aquifer. In this case, the imbibition front (the portion of the interface where the wetting fluid is advancing) interacts with the left boundary early and begins to rise (Figure 1c). The upward motion of the imbibition front causes an increasing portion of the drainage front (the portion of the interface where the wetting fluid is retreating) to be pinned. Eventually, the entire drainage front is pinned and the nonwetting current is arrested at a finite distance (Figure 1d). We study this system experimentally using analog fluids in flow cells packed with glass beads, as well as in micromodels etched with small cross-stream posts. In contrast to previous studies on immiscible gravity currents, which incorporate capillarity at the continuum scale through a capillary pressure-saturation curve, our experiments are aimed at understanding the physical mechanisms acting at the pore scale. We show how pore-scale mechanisms alter the behavior of immiscible gravity currents at the macroscopic scale. We extend the classical model of gravity currents in porous media [Huppert and Woods, 1995; Hesse *et al.*, 2007] to include capillary pinning and nose blunting and demonstrate how both mechanisms limit the spreading of a nonwetting current.

## 2. Laboratory Experiments in Porous Media

In this section, we present our observations from laboratory experiments in porous media. In the next section, we connect these macroscopic observations with pore-scale mechanisms. We consider the instantaneous release of a finite volume of buoyant nonwetting fluid into a horizontal aquifer filled with a relatively dense wetting fluid. We conduct these experiments in a rectangular, quasi two-dimensional flow cell packed with approximately monodisperse spherical glass beads, following the same procedure described in Zhao *et al.* [2013]. The cell is 5.2 cm tall and 56 cm long, with a thickness of 1 cm. We use air as the buoyant nonwetting fluid, paired with one of three dense wetting fluids (Table 1). We report the measured porosity and effective permeability of the bead packs in Table 2. We release the same volume of air in every experiment, fixing the width of the initial release,  $l = 4.9$  cm (Figure 2).

buoyant fluid and the ambient fluid: the capillary fringe.

Continuum-scale models predict that capillary effects result in a thick nonwetting current with a blunt nose [Lake, 1989; Nordbotten and Dahle, 2011; Golding *et al.*, 2013].

Zhao *et al.* [2013] performed the first laboratory experiments of immiscible gravity-exchange flow of two immiscible fluids in porous media. Focusing on the early time evolution of the macroscopic interface between the fluids, they observed a phenomenon they coined capillary pinning, where a portion of the macroscopic fluid-fluid interface remains stationary (Figures 1a and 1b). They identified pore-scale capillary pressure hysteresis between drainage and imbibition as the mechanistic cause of the pinned interface. While Zhao

**Table 1.** Properties of the Three Ambient Fluids Used in the Experiments

Ambient Fluid	$\rho$ (g/cm <sup>3</sup> )	$\mu$ (g/cm s)	$\gamma$ (dyn/cm)
Silicone oil	0.96	0.48	20
Propylene glycol	1.04	0.46	36
Glycerol-water mixture	1.2	0.47	65

### 2.1. Capillary Pinning and Depinning

Starting from the initial condition of a vertical interface separating the buoyant, nonwetting fluid and the dense, wetting fluid, the two fluids first undergo

a gravity-exchange flow. During this early period, we observe that a portion of the initial interface is pinned and does not experience any macroscopic motion (Figures 1a and 1b). The pinning of the initial interface during the exchange flow was described by *Zhao et al.* [2013]. Here we study the flow behavior after the end of the exchange flow, at which point the wetting fluid reaches the left boundary of the flow cell and the imbibition front starts to rise (Figures 1c and 1d). The rise of the imbibition front is accompanied by depinning at the bottom of the vertical pinned interface. As the imbibition front rises, an increasing portion of the drainage front is pinned. Eventually, the spreading of the gravity current stops when the entire drainage front is pinned. This is in stark contrast with miscible gravity currents, which spread indefinitely [*Huppert and Woods, 1995; Hesse et al., 2007*].

### 2.2. Nose Blunting

In miscible gravity currents between a buoyant, less viscous fluid and a dense, more viscous fluid, the buoyant fluid spreads out as a thin tongue, with nose thickness on the scale of one grain diameter [*MacMinn and Juanes, 2013*]. In immiscible gravity currents, in contrast, we observe a blunted nose at the front of the buoyant, nonwetting current, as well as a thick current profile (Figure 1d).

## 3. Micromodel Experiments and Pore-Scale Mechanisms

In this section, we connect the macroscopic observations from the previous section with their pore-scale origins.

### 3.1. Capillary Pinning and Depinning

*Zhao et al.* [2013] studied the early stage (exchange flow) of immiscible gravity currents in porous media and found that the strength of capillary pinning, as measured by the length of the pinned portion of the interface, is a function of the relative importance between capillarity and gravity, as described by the inverse of the Bond number,

$$Bo^{-1} = \frac{\gamma/d}{\Delta\rho gH}, \tag{1}$$

where  $\gamma$  is the interfacial tension between the fluids,  $d$  is the characteristic grain size of the bead pack,  $\Delta\rho$  is the density difference between the fluids,  $g$  is the gravitational constant, and  $H$  is the height of the flow cell (Figure 3).

To understand the mechanistic cause of the pinned interface, we conduct experiments with air and silicone oil in micromodels made of thin acrylic plates etched with cylindrical posts on a rectangular lattice (Figure 4). The micromodels serve as a porous medium analog in the sense of introducing microstructure, while permitting clear visualization of the flow at the pore level. In particular, the pore level fluid-fluid interface is a direct indication of the magnitude of capillary pressures locally. The capillary pressure at each pore throat is given by the Laplace pressure  $P_c = \gamma(R_1^{-1} + R_2^{-1})$ , where  $R_1$  is the radius of curvature of the fluid-fluid interface in the plane orthogonal to the axes of the cylindrical posts and  $R_2$  is the radius of curvature of the

fluid-fluid interface in the quasi two-dimensional plane. The transition of the pore-scale radius of curvature along the pinned vertical interface clearly indicates the presence of capillary pressure hysteresis between

**Table 2.** Properties of the Three Bead Packs Used in the Experiments

Bead Size (cm)	$d$ (cm)	$\phi$ (-)	$k$ (cm <sup>2</sup> )
0.08–0.12	0.1	0.407	$0.9 \times 10^{-5}$
0.1–0.15	0.125	0.412	$1.3 \times 10^{-5}$
0.15–0.2	0.175	0.437	$4.5 \times 10^{-5}$

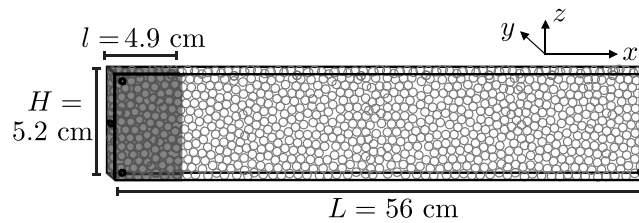


**Figure 2.** Schematic of the laboratory experiments in porous media. We conduct experiments in quasi two-dimensional flow cells packed with glass beads with an initial release of a rectangular volume of buoyant, nonwetting fluid (gray) into a dense, wetting fluid (white).

pressure implies that the height of the pinned interface is given by  $\Delta h_c = \Delta P_c / \Delta \rho g$ . Since  $p_c^{dr}, p_c^{imb} \sim \gamma/d$ ,  $\Delta h_c/H$  scales linearly with  $Bo^{-1} = (\gamma/d) / (\Delta \rho g H)$  (Figure 3).

After the dense wetting current reaches the left boundary of the flow cell, the bottom of the vertical pinned interface starts to depin and becomes part of the imbibition front. This results in a reduced vertically pinned interface. Since the amount of capillary pressure hysteresis in the system remains the same, the hydrostatic pressure increase along the now reduced vertical pinned interface only accounts for part of the entry-pressure difference between drainage and imbibition. At the pore scale, this is reflected by the larger radius of curvature at the top of the vertical pinned interface compared to that at the end of the exchange flow stage (Figure 4b). To balance capillary pressure hysteresis, the pinned interface moves upward and extends into the drainage front. The depinning of the previously pinned interface and the pinning of the previously draining interface are synchronized with each other such that the height difference between the top and the bottom of the pinned interface is always the same,  $\Delta h_c$ . Eventually, the current stops when the entire drainage front becomes pinned.

### 3.2. Nose Blunting

We measure the thickness of the leading edge, or “nose,” of the nonwetting current in the porous media experiments,  $h_n$ , and find that for a given bead pack,  $h_n$  increases with  $Bo^{-1}$ . To expand on this observation, we conduct experiments in the micromodel used in Zhao *et al.* [2013]. The micromodel consists of evenly spaced, uniformly sized cylindrical posts such that the pore-throat size is the same everywhere. We

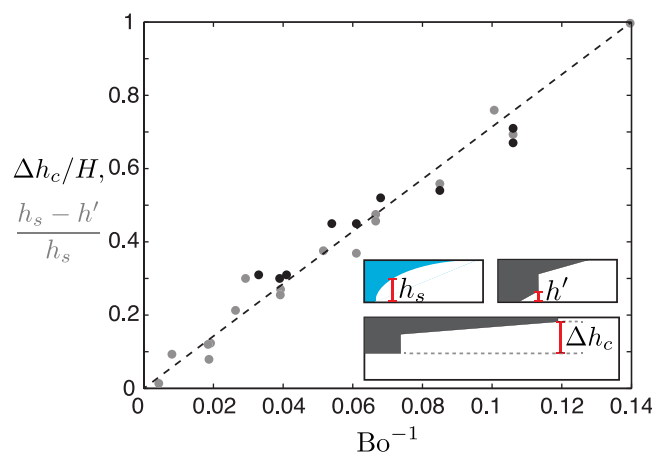


**Figure 3.** Scaling of the pinned interface height and the nose thickness. In contrast to miscible gravity currents, which spread indefinitely, immiscible gravity currents stop at a finite distance. We measure the height difference between the highest point and the lowest point of the nonwetting current,  $\Delta h_c$  (inset), after the current stops and find that it scales linearly with the strength of capillary relative to gravity, as measured by  $Bo^{-1}$ , normalized by the height of the cell  $H$  (black circles). The slope of this linear scaling matches that of the capillary height reported in Zhao *et al.* [2013] (gray circles), defined as the normalized difference between the lower hinge height  $h'$  and the height of the miscible tilting point,  $h_s$  (inset).

drainage and imbibition (Figure 4a). Along the vertical pinned interface, the capillary pressure decreases with depth from the drainage capillary pressure  $p_c^{dr}$  to the imbibition capillary pressure  $p_c^{imb}$ . This decrease in capillary pressure,  $\Delta P_c = p_c^{dr} - p_c^{imb} > 0$ , is offset by the increase in hydrostatic pressure along the vertical, pinned interface. The balance between these two changes in

pressure implies that the height of the pinned interface is given by  $\Delta h_c = \Delta P_c / \Delta \rho g$ . Since  $p_c^{dr}, p_c^{imb} \sim \gamma/d$ ,  $\Delta h_c/H$  scales linearly with  $Bo^{-1} = (\gamma/d) / (\Delta \rho g H)$  (Figure 3).

will refer to this micromodel as the “uniform micromodel.” We conduct gravity current experiments under a wide range of  $Bo^{-1}$  by tilting the micromodel about the  $x$  axis, thus changing the effective strength of gravity in the  $y$ - $z$  plane. We do not observe nose blunting in the uniform micromodel even when the effective gravity is low compared to capillarity (i.e., large  $Bo^{-1}$ ; Figure 5a).

The absence of nose blunting in the uniform micromodel suggests that  $Bo^{-1}$  alone is not sufficient to explain nose blunting and that some additional parameter, possibly the pore geometry, is also important. To test this hypothesis, we perform the same experiments in a micromodel with anisotropic pore-throat

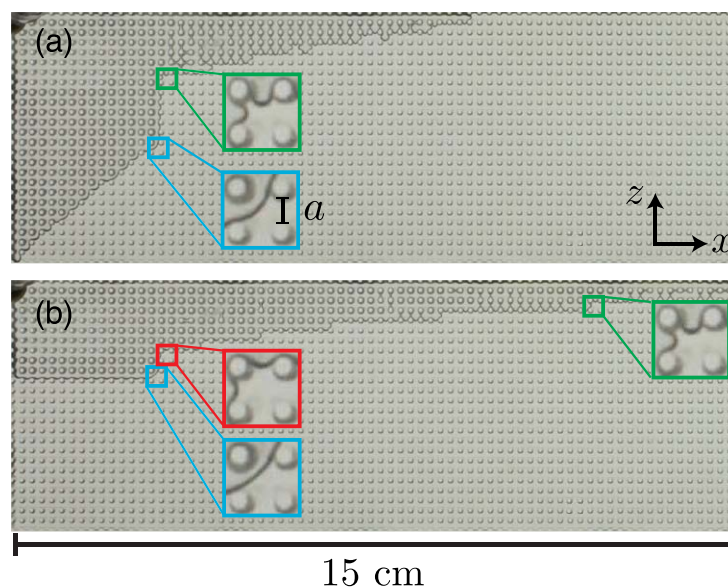


**Figure 4.** Visualization and physical mechanism of capillary pinning. (a) Snapshot of the exchange flow phase of an immiscible gravity current between air and silicone oil in a micromodel with uniform pore-throat size ( $a = 1$  mm). Capillary pressure hysteresis between drainage (green) and imbibition (blue) is visible via the increase in the radius of curvature of the pore-scale fluid-fluid interface along the vertical interface. The portion of the interface between drainage and imbibition is pinned and does not move during the exchange flow. (b) Snapshot of the finite-release phase of the same gravity current. During the finite-release phase, the imbibition front rises, which leads to a reduced vertical interface. The radius of curvature of the fluid-fluid interface at the top of the vertical interface has increased, indicating that it is now pinned (red). The reduction in the vertical pinned interface is offset by the extension of the pinned interface to the right, pinning increasingly larger portion of the drainage front. The current stops when the entire drainage front is pinned.

is visible via the change in the radius of curvature of the pore-scale fluid-fluid interface along the nose (Figure 5b).

To draw the connection with the observations in porous media, we perform experiments in micromodels with disorder in the microstructure (Figure 6). Here we randomly assign the pore-throat radii by drawing from a uniform distribution with a range of  $a \in [0.25, 0.75]$  mm. We will refer to this micromodel as the “random micromodel.” In this system, even though the pore-throat sizes are random and anisotropy is absent, we still observe a blunted nose that thickens with increasing  $Bo^{-1}$ . In addition, the disorder in the pore-throat sizes leads to a rough drainage front (Figure 6), which is also observed in the porous media experiments.

We now derive a quasi static, invasion percolation-type model [Wilkinson and Willemsen, 1983; Lenormand et al., 1988; Cieplak and Robbins, 1990] to numerically simulate the drainage sequence in the random micromodel. In order for a fluid-fluid interface at a given pore throat to advance to the adjacent pore, the air pressure must be greater than the sum of the local drainage capillary entry pressure and the hydrostatic pressure in the liquid  $P_a > P_{c,e}^{dr} + P_l$ . Since the contact angle between silicone oil and air on an acrylic substrate is zero, the drainage capillary entry pressure is  $P_{c,e}^{dr} \approx 2\gamma(a^{-1} + d^{-1})$ , where  $a$  is the width of the throat between neighboring posts and  $d$  is the height of the posts [Lenormand et al., 1983]. We assume that the air pressure is the same everywhere and that the oil pressure is hydrostatic. At each step, we calculate  $P_{c,e}^{dr} + P_l$  at every fluid-fluid interface and advance the interface with the smallest  $P_{c,e}^{dr} + P_l$  to the neighboring pore.

We find that our simple model is able to accurately capture the drainage sequence in the random micromodel experiments at late times, when viscous effects are small (Figure 6). The relative importance between capillary forces and viscous forces is described by the capillary number  $Ca = \mu U / \gamma$ , where  $\mu$  is the viscosity of the dense, more viscous fluid, and we use the rate of nose advancement as the characteristic velocity  $U$ . As the viscous effects become small, drainage of the nonwetting phase is completely

sizes such that the horizontal pore throats are larger than those in the vertical direction. We will refer to this micromodel as the “anisotropic micromodel.” We observe nose blunting in the anisotropic micromodel (Figure 5b) and find that the nose thickness increases with increasing  $Bo^{-1}$ . The presence of nose blunting in the anisotropic micromodel is similar to that of the vertical pinned interface in the sense that along the blunted nose, the drainage capillary pressure transitions from the entry pressure needed to invade the smaller, vertical pore throats at the top to the entry pressure needed to invade the larger, horizontal pore throats at the bottom. This transition in capillary pressure is balanced by the hydrostatic pressure increase across the blunted nose and

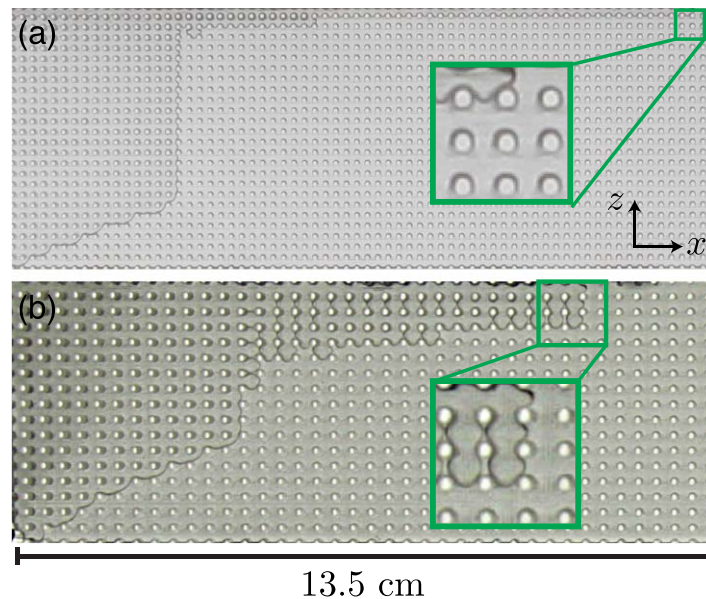


**Figure 5.** Visualization and mechanistic origin of nose blunting. (a) Snapshot of an immiscible gravity current between air and silicone oil in a micromodel with uniform pore-throat size ( $a = 1$  mm). A significant portion of the initial interface is pinned, indicating strong capillarity with respect to gravity. Yet the nose of the nonwetting current spreads only along the top row of the micromodel. (b) Snapshot of an immiscible gravity current experiment between air and silicone oil in a micromodel with anisotropic pore-throat size distribution. The pore throats parallel to the  $x$  axis are 2 mm wide, while the pore throats parallel to the  $z$  axis are 1.5 mm wide. The anisotropic pore-throat size distribution creates anisotropy in the capillary entry pressure. Along the nose, the capillary pressure transitions hydrostatically from the larger capillary entry pressure required for air to drain forward, to the smaller capillary entry pressure required for air to drain downward. This is reflected by the change in radius of curvature of the pore-scale fluid-fluid interface along the nose.

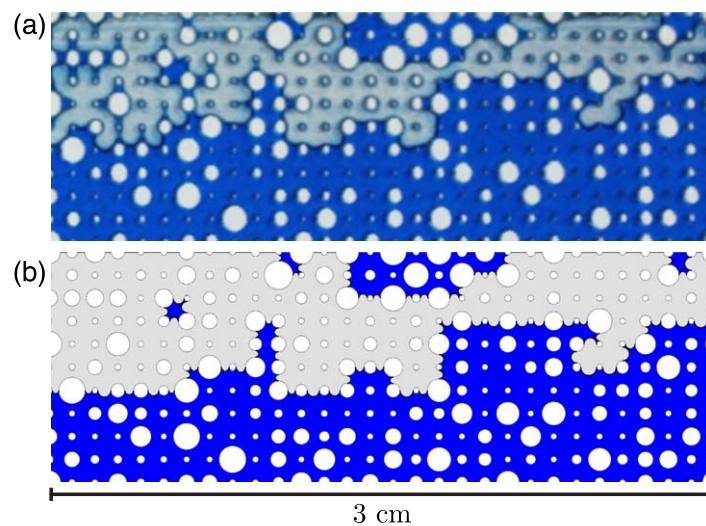


**Figure 6.** Thickness and roughness of the nose of a gravity current. (a) The nose of an immiscible gravity current experiment of air spreading over silicone oil in a thin acrylic cell with round posts etched on a rectangular grid. The pore-throat sizes are randomized and follow a uniform distribution within the range of  $a \in [0.25, 0.75]$  mm. (b) We simulate the drainage process of the micromodel experiment using the quasi-static model. The quasi-static model is able to accurately capture the drainage process of the gravity current at late times, when viscous effects are negligible ( $Ca=0.0024$ ). Here the differences in capillary pressures at the drainage front are balanced by gravity, resulting in a characteristic thickness of the nonwetting current, even though the interface between the fluids is rough. Videos of the micromodel experiment and the quasi-static model simulation are provided in the supporting information.

controlled by capillarity and gravity. This regime is characterized by previous studies as gravity-capillary equilibrium [Lake, 1989; Zhou et al., 1997; Yortsos, 1995; Golding et al., 2011; Nordbotten and Dahle, 2011; Golding et al., 2013]. Since the quasi-static model only takes into account of the local capillary entry pressure and the hydrostatic pressure, its ability to predict the drainage sequence shows that nose blunting is strongly influenced by the spatial distribution of pore-throat sizes and hence, different capillary entry pressures: forward drainage of the nonwetting fluid is temporarily stalled at narrow pore throats, as downward drainage through wider pore throats becomes more favorable. Videos showing the comparison between a random micromodel experiment and the quasi-static model simulation are provided in the supporting information. We find that the anisotropy of the pore space has negligible effects on the imbibition front. This is because the imbibition front advances through cooperative invasion of multiple pores simultaneously, whereas the drainage front relies on subsequent invasion of individual pores [Cieplak and Robbins, 1990].

Since nose blunting is caused by the spatial distribution of capillary entry pressures, we can define a characteristic maximum capillary entry pressure  $P_{c,e}^{\max}$  and a characteristic minimum capillary entry pressure  $P_{c,e}^{\min}$ . The difference

between the two characteristic capillary entry pressures is balanced by the increase in hydrostatic pressure along the nose of the current and the nose thickness is given by

$$h_n = \frac{p_{c,e}^{\max} - p_{c,e}^{\min}}{\Delta\rho g} + h_o, \quad (2)$$

where  $h_o$  is some base nose thickness, which is on the order of a single bead. We scale  $h_n$  and  $h_o$  by the cell height such that  $h'_n = h_n/H$ ,  $h'_o = h_o/H$ , and  $p_{c,e}^{\max}$  and  $p_{c,e}^{\min}$  by the Laplace pressure such that  $P'_{c,\max} = p_{c,e}^{\max}/(\gamma d^{-1})$  and  $P'_{c,\min} = p_{c,e}^{\min}/(\gamma d^{-1})$ . We obtain

$$h'_n = \frac{\gamma/d}{\Delta\rho g H} (P'_{c,\max} - P'_{c,\min}) + \frac{h_o}{H}. \quad (3)$$

The first term on the right-hand side of equation (3) is equal to  $\text{Bo}^{-1}\zeta$ , where we define  $\zeta = P'_{c,\max} - P'_{c,\min}$ , which measures the amount of disorder in the pore-throat size distribution. A larger value of  $\zeta$  corresponds to a wider pore-throat size distribution, and hence, a more blunted nose for a given  $\text{Bo}^{-1}$ . For aquifers where  $H \gg d$ ,  $h_o$  becomes negligible and the dimensionless nose height  $h'_n$  is given by

$$h'_n \approx \text{Bo}^{-1}\zeta. \quad (4)$$

#### 4. Macroscopic Sharp-Interface Model

We propose a macroscopic model that predicts the evolution, and eventually the stopping of immiscible finite-release gravity currents. We base our model on the classical sharp-interface model [Huppert and Woods, 1995; Yortsos, 1995; Hesse et al., 2007], which assumes hydrostatic pressure distribution everywhere. The classical formulation describing miscible gravity currents [Huppert and Woods, 1995] is a partial differential equation for the height of the fluid-fluid interface, and is given by

$$\frac{\partial h}{\partial t} - \kappa \frac{\partial}{\partial x} \left[ (1-f)h \frac{\partial h}{\partial x} \right] = 0, \quad (5)$$

where  $h(x, t)$  is the height of the fluid-fluid interface measured from the bottom of the aquifer,  $\kappa = \Delta\rho g k/(\mu\phi)$  is the characteristic buoyancy velocity, and  $f(h)$  is the so-called fractional flow function and is given by

$$f = \frac{h}{h + \mathcal{M}(H-h)}, \quad (6)$$

with  $\mathcal{M}$  being the viscosity ratio between the fluids.

The classical formulation can be extended to include capillary effects based on the concept of macroscopic capillarity [Nordbotten and Dahle, 2011; Golding et al., 2011, 2013], where one assumes that capillary pressure is a function of the nonwetting phase saturation [Leverett, 1941]. To relate fluid saturation to capillary pressure, they use empirical models for capillary pressure curves such as the Brooks-Corey model [Brooks and Corey, 1966] and the van Genuchten model [van Genuchten, 1980]. They further assume gravity-capillary equilibrium ( $\partial P_c/\partial z = \Delta\rho g$ ) to relate fluid saturation and height of the fluid-fluid interface. The gravity-capillary equilibrium assumption predicts a capillary fringe, or transition zone, where the nonwetting phase saturation varies considerably with respect to depth. The resulting formulation is a vertically integrated model for the interface height that reduces to the classical sharp-interface model for single-phase gravity current in the absence of capillarity. This type of model shows that the existence of a capillary fringe could significantly impact the migration of two-phase gravity currents, and it predicts that capillary effects create a thick current as well as a rounder nose profile [Nordbotten and Dahle, 2011; Golding et al., 2011, 2013]. These models, however, assume that capillary pressure is a unique function of the nonwetting phase saturation only, and therefore, do not capture the hysteretic nature of capillary pressure. As a result, they do not reproduce interface pinning and finite spreading of two-phase gravity currents.

Capillary pressure hysteresis has been recently incorporated in vertically integrated models of two-phase flow in porous media [Zhao et al., 2013; Doster et al., 2013]. Doster et al. [2013] study the impact of

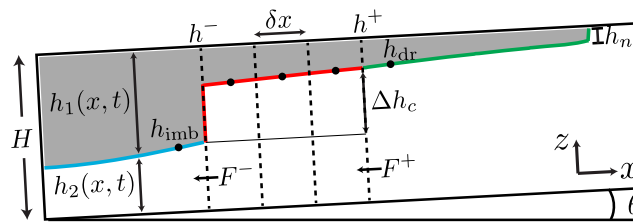


**Figure 7.** Macroscopic sharp-interface model for immiscible gravity currents that includes capillary pinning and blunting. After the dense, wetting fluid hits the left boundary, the imbibition front (blue line) starts to move up, causing the active drainage front (green line) to become progressively pinned. As a result, the length of the pinned interface (red line) grows with time, such that the height difference between the imbibition front and drainage front is always  $\Delta h_c$ . The buoyant current stops spreading when the entire drainage front becomes pinned. The model also enforces the leading edge of the buoyant current to fill downward to the characteristic nose height  $h_n$  before advancing forward. We solve the model numerically using a finite volume scheme. This figure illustrates how we incorporate the pinned interface into our numerical scheme as explained in Appendix A, with solid circles being cell centers and dashed line being cell interfaces.

the current as well as progressive pinning of the drainage front, which is ultimately responsible for stopping the migration of the gravity current.

#### 4.1. Mathematical Model

We consider an immiscible gravity current between a buoyant nonwetting fluid with density  $\rho$  and a dense wetting fluid with density  $\rho + \Delta\rho$  in an inclined porous medium of thickness  $H$  and slope  $\theta$  (Figure 7). We assume that the porous medium is homogeneous and isotropic with permeability  $k$  and porosity  $\phi$  and that the boundaries of the flow domain are impermeable. Since we assume that the two fluids are separated by a sharp interface, the thickness of the fluid layers must sum to the thickness of the porous layer everywhere,  $h_1 + h_2 = H$ . By assuming hydrostatic pressure in both fluids, we can express the pressure distribution in the layer as

$$P = \begin{cases} P_i - \rho g \cos \theta (z - h_2) & \text{for } z > h_2 \\ P_i - P_c + (\rho + \Delta\rho) g \cos \theta (h_2 - z) & \text{for } z \leq h_2 \end{cases}, \quad (7)$$

where  $P_i$  is the unknown pressure at the interface and  $g$  is the gravitational acceleration. By definition, the pressure difference across the interface between the nonwetting fluid and the wetting fluid is the capillary pressure  $P_c$ .

The volumetric flux per unit width of fluid phase  $i$  along the slope is given by Darcy's law  $q_i = -k\lambda_i(\partial P/\partial x - \rho_i g \sin \theta)$ , where  $\lambda_i = k_{ri}/\mu_i$  and  $\rho_i$  are the mobility and density of the fluid phase, and  $k_{ri}$  is the relative permeability to that phase. Since we assume the two fluid phases to be completely segregated and the fluid saturation to be homogeneous within each layer, the relative permeabilities are constant. The flow rate is given by the product of the thickness of the fluid phase and its volumetric flux,  $Q_i = h_i q_i$ ,

$$Q_1 = -h_1 k \lambda_1 \left[ \frac{\partial P_i}{\partial x} - \rho g \left( \cos \theta \frac{\partial h_1}{\partial x} - \sin \theta \right) \right], \quad (8a)$$

$$Q_2 = -h_2 k \lambda_2 \left[ \frac{\partial P_i}{\partial x} - \frac{\partial P_c}{\partial x} - (\rho + \Delta\rho) g \left( \cos \theta \frac{\partial h_2}{\partial x} - \sin \theta \right) \right]. \quad (8b)$$

We solve for  $\partial P_i/\partial x$  by imposing global volume conservation  $Q_1 + Q_2 = 0$ . We then substitute  $\partial P_i/\partial x$  into equation (8) and, enforcing the identity  $h_1 + h_2 \equiv H$ , we can express the flow rates in terms of only  $h_2$ , which also represents the height of the interface:

$$Q_2 = \frac{\Delta\rho g k}{\mu_2} (1-f) h_2 \left( \cos \theta \frac{\partial h_2}{\partial x} + \sin \theta - \frac{\partial P_c/\Delta\rho g}{\partial x} \right), \quad (9a)$$

capillary pressure hysteresis and residual trapping on the constitutive parameter functions of the vertically integrated models. Zhao et al. [2013] study two-phase exchange flow in horizontal porous layers. They incorporate capillary pressure hysteresis to the classical sharp-interface model by introducing a capillary term in the flux function that captures capillary pinning. The resulting model reproduces the pinned interface as well as the early time spreading dynamics. Here, we extend this model to an inclined aquifer and we include blunting at the nose of

$$f = \frac{h_2}{h_2 + \mathcal{M}(H - h_2)}, \tag{9b}$$

where  $f$  is the fractional flow function and  $\mathcal{M} = \lambda_1 / \lambda_2$  is the mobility ratio. To obtain an equation for the evolution of the interface, we consider the conservation of volume of the dense fluid over region  $\Delta x$  and time  $\Delta t$ . The change in volume of the dense fluid is given by

$$\Delta V_2 = \Delta h_2 \Delta x (1 - S_{wc}) \phi = (Q_2|_{x+\Delta x} - Q_2|_x) \Delta t, \tag{10}$$

where  $S_{wc}$  is the connate water saturation, which accounts for the fact that the nonwetting current does not displace all the wetting fluid on the drainage front. Inserting equation (9) into equation (10) and taking limits for small  $\Delta x$  and  $\Delta t$ , we obtain the partial differential equation for the evolution of the interface height  $h \equiv h_2$ :

$$\frac{\partial h}{\partial t} - \kappa \frac{\partial}{\partial x} \left[ \frac{(1-f)}{(1-S_{wc})} h \left( \frac{\partial h}{\partial x} + \tan \theta - \frac{\partial h_c}{\partial x} \right) \right] = 0, \tag{11}$$

where we define  $\kappa = \Delta \rho g \cos \theta k / (\mu_2 \phi)$  as the characteristic buoyancy velocity and  $h_c = P_c / (\Delta \rho g \cos \theta)$  as the characteristic height of capillary pressure hysteresis.

It remains to write the capillary pressure,  $P_c$ , in terms of the evolution of the interface. Along the imbibition front, we take the capillary pressure to be constant and equal to a characteristic imbibition capillary pressure,  $P_c^{\text{imb}}$ . Along the drainage front (except for the nose region, which we handle separately), we take the capillary pressure to be constant and equal to a characteristic drainage capillary pressure,  $P_c^{\text{dr}}$ . Along the pinned interface, which connects the imbibition front to the drainage front, the capillary pressure transitions accordingly from its imbibition value to its drainage value. The transition in capillary pressure is offset by the change in hydrostatic pressure along the pinned interface, with a corresponding difference in interface height of  $\Delta h_c = (P_c^{\text{dr}} - P_c^{\text{imb}}) / \Delta \rho g \cos \theta$  between the two ends of the pinned interface. We assume a similar transition at the nose, which we define as the region where the current is thinner than the nose height ( $H - h < h_n$ ), and within which the capillary pressure transitions from  $P_{c,e}^{\text{min}}$  to  $P_{c,e}^{\text{max}}$  with a corresponding change in thickness  $h_n - h_0$  (see section 3.2). We then have that  $\partial h_c / \partial x = 0$  along the imbibition drainage front and along the drainage front, whereas  $\partial h_c / \partial x = \partial h / \partial x$  along the pinned interface and at the nose.

We write the model in dimensionless form by scaling  $h$ ,  $\Delta h_c$ , and  $x$  by the characteristic length  $H$  and  $t$  by the characteristic time  $T = H / \kappa$ , to obtain a partial differential equation describing the dimensionless interface height with respect to dimensionless time

$$\frac{\partial h}{\partial t} - \frac{\partial}{\partial x} \left[ \frac{(1-f)}{(1-S_{wc})} h \left( \frac{\partial h}{\partial x} + \tan \theta - \frac{\partial h_c}{\partial x} \right) \right] = 0, \tag{12}$$

where we substitute each variable in equation (11) with its dimensionless counterpart.

### 5. Spreading Dynamics

Hesse *et al.* [2007] developed early and late-time similarity solutions for the spreading of a miscible gravity current in a horizontal porous layer. They found that the tip of the buoyant current (the nose position) propagates as  $x_n \sim t^{1/2}$  during early times, when the released fluid fills the entire height of the aquifer, and later as  $x_n \sim t^{1/3}$ , when the height of the released fluid is much smaller than the thickness of the aquifer. They found that the time it takes for the late-time scaling of the nose position to become valid (the transition time) is a function of the mobility ratio  $\mathcal{M}$ , such that the transition time is longer with higher  $\mathcal{M}$ .

The nose positions measured from our experiments initially follow the same  $x_n \sim t^{1/2}$  scaling as the early time behavior of their miscible counterpart [Hesse *et al.*, 2007] (Figure 8). The  $x_n \sim t^{1/3}$  scaling is absent because of the large mobility ratios in our experiments ( $\mathcal{M} \sim 2500$ ) and the relatively large value of  $\text{Bo}^{-1}$ , such that current migration is stopped before the transition from early time scaling ( $x_n \sim t^{1/2}$ ) to late-time scaling ( $x_n \sim t^{1/3}$ ) is reached. Using our macroscopic sharp-interface model, we find that the  $x_n \sim t^{1/3}$  spreading regime does exist in immiscible gravity currents, but only for those at small  $\text{Bo}^{-1}$  and small  $\mathcal{M}$ , after a

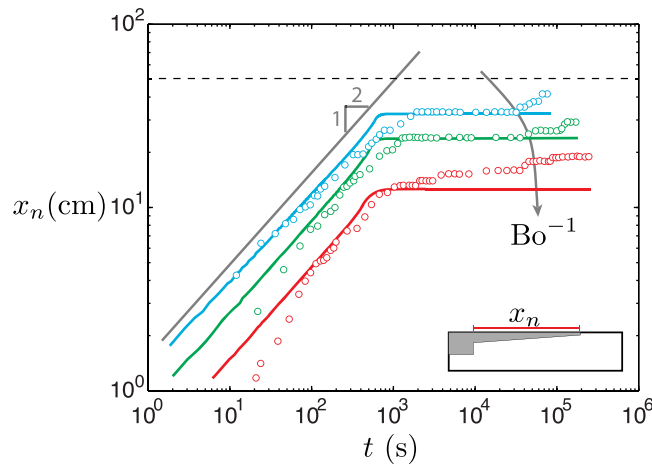


**Figure 8.** Spreading dynamics of immiscible gravity currents in horizontal porous layers. Time evolution of the nose positions of air spreading over silicone oil (blue circles;  $Bo^{-1}=0.033$ ), propylene glycol (green circles;  $Bo^{-1}=0.054$ ), a glycerol-water mixture (red circles;  $Bo^{-1}=0.085$ ) show immiscible gravity currents initially follow the same  $x_n \sim t^{1/2}$  scaling as their miscible counterparts. The stopping distance of the buoyant current as well as its rate of advancement decreases with increasing  $Bo^{-1}$ . The gray dashed line represents the right boundary of the flow cell. The solid lines represent the simulated nose positions from the sharp-interface model. The apparent long-time scale adjustments of the nose positions after complete pinning of the gravity current are related to throat widening due to the slow gravity drainage of the wetting films coating the glass beads in the drained region, which effectively decreases the value of  $\Delta h_c$ .

miscible current, which in the sharp-interface limit continues to spread forever. The mechanistic cause of the finite migration distance is capillary pressure hysteresis: the current stops when the height difference between the imbibition front and the drainage front reaches  $\Delta h_c = \Delta P_c / \Delta \rho g$ . As a result, the stopping distance  $x_f$  is a monotonically decreasing function of  $Bo^{-1}$ .

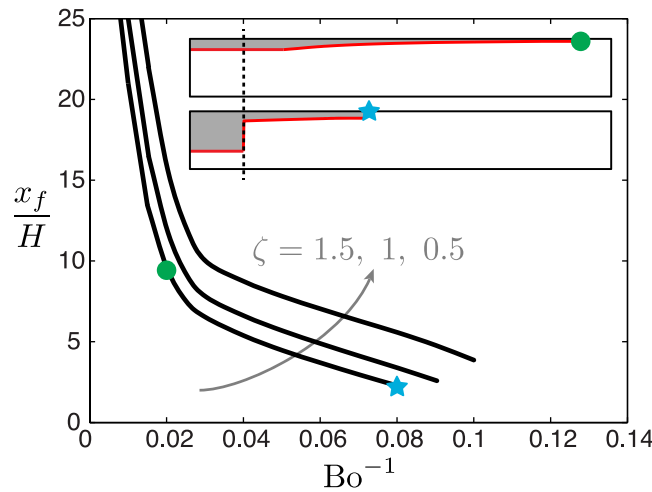


**Figure 9.** Stopping distance of an immiscible gravity current. The stopping distance is controlled by both capillary pinning and nose blunting. While both processes depend on  $Bo^{-1}$ , nose blunting is also strongly influenced by the pore geometry. Here we plot the dimensionless stopping distance  $x_f/H$  as a function of  $Bo^{-1}$  of a square-shaped release of nonwetting fluid. The stopping distances are obtained from our macroscopic sharp-interface model, for  $\mathcal{M}=2500$  and three different  $\zeta$  values. As expected, the stopping distance approaches infinity as capillarity becomes negligible and it tends to zero as capillarity is increased to the limit of complete pinning. The “kink” in the curves above occurs at sufficiently small  $Bo^{-1}$  such that the initial vertical interface completely depins and the imbibition front is able to expand outward before the current stops. The final state of the current at large and small  $Bo^{-1}$  is illustrated in the figure inset. The vertical dashed line in the inset shows the initial width of the nonwetting fluid.

sufficiently long time. For immiscible gravity currents at high  $Bo^{-1}$ , the initial vertical interface never gets completely depinned and, hence, the buoyant current never gets truly thin compared to the height of the aquifer—as a result, it never enters the  $x_n \sim t^{1/2}$  spreading regime.

Although capillarity does not change the scaling of the nose positions with respect to time, it does cause a reduction in the rate of propagation of the gravity current: the speed of propagation decreases with higher  $Bo^{-1}$  (Figure 8).

The most striking feature in the spreading dynamics of an immiscible gravity current is that the current stops at a finite distance, as opposed to a

monotonically decreasing function of  $Bo^{-1}$ . The relationship between  $x_f$  and  $Bo^{-1}$ , however, is markedly nonlinear. At sufficiently low  $Bo^{-1}$ , the entire initial vertical interface depins and the imbibition front expands laterally outward. This allows the wetting fluid to displace a much larger volume of the nonwetting fluid that would otherwise be “trapped” by the vertical pinned interface at higher  $Bo^{-1}$ . As a result,  $x_f$  increases significantly at low  $Bo^{-1}$  such that it approaches infinity when capillarity is negligible (Figure 9). In addition to  $Bo^{-1}$ ,  $x_f$  is also a function of the pore-throat size distribution of the porous medium, as characterized by the “pore-scale disorder” parameter  $\zeta$  (section 3.2). Higher  $\zeta$  represents a wider pore-throat size distribution, which causes

**Table 3.** Geologic Formations Associated With Actual CO<sub>2</sub> Sequestration Projects, to Which We Apply Our Model

Aquifer	$H$ (m)	$k$ (m <sup>2</sup> )	$S_{gr}$ (-)	$S_{wc}$ (-)	$Bo^{-1}$ (-)	$\Gamma$ (-)	References
Otway	25	$7 \times 10^{-13}$	0.33	0.09	$9.9 \times 10^{-3}$	0.33	Hortle et al. [2009] and Underschultz et al. [2011]
Tuscaloosa	60	$2.2 \times 10^{-13}$	0.31	0.05	$7.4 \times 10^{-3}$	0.37	Kuuskraa et al. [2009] and Krevor et al. [2012]
Mt. Simon	100	$1 \times 10^{-13}$	0.3	0.4	$6.6 \times 10^{-3}$	0.5	Szulczewski et al. [2012]
Teapot Dome	30	$3 \times 10^{-14}$	0.3	0.4	$4.0 \times 10^{-2}$	0.5	García [2005] and Chieramonte et al. [2008]

more vertical drainage as the nonwetting fluid spreads outward. The increase in vertical extent of the nonwetting current reduces its lateral extent, leading to a shorter stopping distance (Figure 9).

### 6. Application to Carbon Sequestration

Geologic CO<sub>2</sub> sequestration relies on trapping mechanisms to securely store the injected CO<sub>2</sub>. These mechanisms include residual trapping, where tiny blobs of CO<sub>2</sub> are immobilized by capillary forces [IPCC, 2005; Juanes et al., 2006], and solubility trapping, where CO<sub>2</sub> dissolves into the ambient groundwater [IPCC, 2005]. Recent studies have shown that convective dissolution, where free-phase CO<sub>2</sub> is carried away from the buoyant CO<sub>2</sub> current, can greatly enhance the rate of solubility trapping [Weir et al., 1996; Lindeberg and Wessel-Berg, 1997; Riaz et al., 2006]. As a result, convective dissolution will eventually arrest the migration of the buoyant CO<sub>2</sub> current [Gasda et al., 2011; MacMinn et al., 2011; MacMinn et al., 2012; MacMinn and Juanes, 2013].

We now apply our model to demonstrate the implications of capillary pinning and blunting in the context of geologic CO<sub>2</sub> sequestration. Specifically, we compare the trapping efficiency of capillary pinning and blunting with the combined effect of residual trapping and convective dissolution. MacMinn et al. [2011] developed a sharp-interface model for the updip migration of a buoyant plume, under the influence of residual trapping and convective dissolution:

$$\tilde{R} \frac{\partial \eta}{\partial \tau} + \frac{\partial}{\partial \zeta} \left[ N_s (1-f') \eta - (1-f') \eta \frac{\partial \eta}{\partial \zeta} \right] = -\tilde{R} N_d, \tag{13}$$

where  $\eta = h_1/H$ ,  $\zeta = x/l$ ,  $f' = \mathcal{M}\eta/[(\mathcal{M}-1)\eta+1]$ , and  $\tau = t/T$ . The model is uniquely characterized by four dimensionless parameters:

1.  $N_s = (l/H)\tan \theta$ , which measures the importance of upslope migration.
2.  $N_d = l^2 q_d / (H^2 \phi \kappa \mathcal{M} \cos \theta)$ , which measures the importance of convective dissolution. The convective dissolution flux per unit area of fluid-fluid interface is  $q_d = \alpha \chi_v \Delta \rho_d g k / \mu_2$ , where  $\chi_v$  measures the maximum equivalent volume of free-phase CO<sub>2</sub> that can dissolve in one unit volume of brine,  $\Delta \rho_d$  is the density difference between brine and CO<sub>2</sub>-saturated brine, and  $\alpha \approx 0.01$  is a constant. The value of  $N_d$  is not dependent on permeability  $k$ , since  $\kappa$  and  $q_d$  are both proportional to  $k$ .
3.  $\tilde{R}$  measures the importance of residual trapping.  $\tilde{R} = 1 - \Gamma$  or 1 locally, depending on whether that portion of the interface is in imbibition or drainage, respectively. The residual trapping number  $\Gamma = S_{gr} / (1 - S_{wc})$  is a function of the residual gas saturation  $S_{gr}$  and the connate water saturation  $S_{wc}$ .
4.  $\mathcal{M}$ , the mobility ratio.

We apply the model with capillary pinning and blunting developed here, as well as the model with residual trapping and convective dissolution developed by MacMinn et al. [2011] to four geologic formations associated with actual CO<sub>2</sub> sequestration projects. We set aquifer thickness  $H$ , permeability  $k$ , residual gas saturation  $S_{gr}$ , and connate water saturation  $S_{wc}$  to values reported in the literature (Table 3). We consider a square-shaped instantaneous release of CO<sub>2</sub> such that  $l = H$ . For simplicity, we fix the aquifer slope  $\theta = 1^\circ$ , pore-scale disorder  $\zeta = 1$ , and the fluid properties of CO<sub>2</sub> and brine to values representative of what could be encountered in deep saline aquifers (Table 4). We obtain  $\mathcal{M} \approx 13$ ,  $N_s \approx 0.017$ ,  $N_d \approx 7.5 \times 10^{-7}$ , while  $Bo^{-1}$  and  $\tilde{R}$  vary based on aquifer-specific properties.

**Table 4.** Fluid Properties Representative of What Could Be Encountered in Deep Saline Aquifers

$\rho_{\text{CO}_2}$ (kg m <sup>-3</sup> )	$\rho_{\text{brine}}$ (kg m <sup>-3</sup> )	$\mu_{\text{CO}_2}$ (Pa s)	$\mu_{\text{brine}}$ (Pa s)	$\Delta\rho_d$ (kg m <sup>-3</sup> )	$\chi_v$ (-)	$\Delta\rho$ (kg m <sup>-3</sup> )	$\mathcal{M}$ (-)
700	1000	$6 \times 10^{-5}$	$8 \times 10^{-4}$	6	0.05	300	13

We use the stopping distance of the CO<sub>2</sub> plume,  $x_f$ , as a measure to compare the trapping efficiency between the combined effect of capillary pinning and blunting, and the combined effect of residual trapping and convective dissolution (Figure 10). As expected, the effect of capillary pinning and blunting is significant for thin, low-permeability aquifers (i.e., high  $\text{Bo}^{-1}$ ), such as the B-sandstone in the Tensleep Formation in the Teapot Dome. Surprisingly, even at thick, high-permeability aquifers (i.e., low  $\text{Bo}^{-1}$ ), capillary pinning and blunting could still be more effective in stopping the CO<sub>2</sub> plume than residual trapping and convective dissolution, as is the case for the Tuscaloosa Formation in the U.S. and the Naylor Field in the CO2CRC Otway Project in Australia. In other cases, however, residual trapping and convective dissolution yield a shorter stopping distance. This is the case for the Mount Simon Sandstone in the U.S., which has a high residual trapping number  $\Gamma$  (low  $\tilde{R}$ ), in addition to being thick and permeable (low  $\text{Bo}^{-1}$ ).

*Szulczewski et al.* [2012] studied eleven of the largest aquifers in the conterminous U.S. as an effort to estimate the CO<sub>2</sub> storage capacity in the country. We find  $\text{Bo}^{-1} \in [1 \times 10^{-4}, 2 \times 10^{-2}]$  in this group of thick and permeable aquifers. *Szulczewski et al.* [2012] estimated  $\Gamma = 0.5$  for all the aquifers they studied because aquifer-specific data on the multiphase flow characteristics of CO<sub>2</sub> and brine were largely unavailable. *Bennion and Bachu* [2008] conducted a series of relative permeability measurements using CO<sub>2</sub> and brine in sandstone samples from Alberta, Canada under reservoir conditions. We combine the values of  $S_{gr}$  and  $S_{wc}$  that they reported with the formations that we considered here and find  $\Gamma \in [0.33, 0.5]$ . Hence, the majority of large-scale CO<sub>2</sub> sequestration projects will likely involve formations that lie in the upper left quadrant of Figure 10. Our analysis shows that capillary pinning and blunting could be an important mechanism in limiting the migration distance of the CO<sub>2</sub> gravity current.

We have assumed here that the aquifer is homogeneous, but all natural rocks are heterogeneous at some scale. Further, the variety of complex pore geometries in natural rocks will lead to quantitatively different results—for example, in terms of the scaling constant for the pinned interface height, and the pore-scale

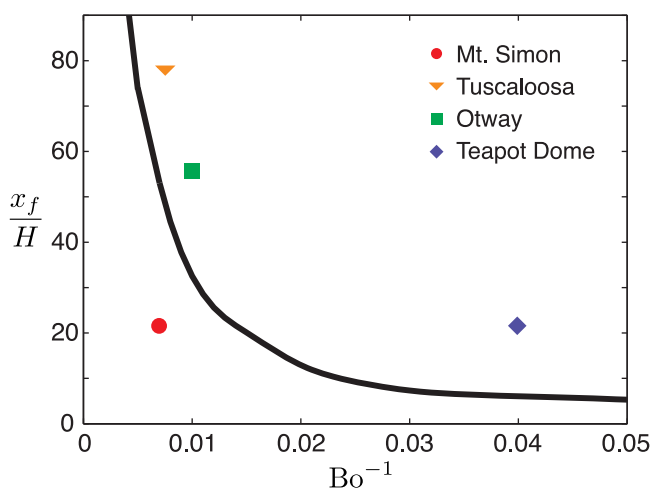


**Figure 10.** Relative importance of capillary pinning and blunting versus residual trapping and convective dissolution in geological CO<sub>2</sub> sequestration. We consider a square-shaped instantaneous release of CO<sub>2</sub> in a weakly sloped aquifer ( $\theta = 1^\circ$ ) and use the dimensionless stopping distance  $x_f/H$  as the metric of comparison. For capillary pinning and blunting, we use the model developed in this paper to obtain  $x_f/H$  as a function of  $\text{Bo}^{-1}$  (solid black line). The symbols show the dimensionless stopping distance of the CO<sub>2</sub> current under the influence of only residual trapping and convective dissolution, as predicted by the model developed by *MacMinn et al.* [2011], using parameters obtained from aquifers associated with real CO<sub>2</sub> sequestration projects. Our analysis shows that capillary pinning and blunting could be just as effective as residual trapping and convective dissolution in limiting the ultimate migration distance of CO<sub>2</sub>.

disorder parameter. Quantifying these parameters for different rock types is beyond the scope of this study, but these considerations are unlikely to have a strong impact on our qualitative findings. It would be useful to include residual trapping, solubility trapping, and capillary pinning and blunting into a single model for CO<sub>2</sub> migration and trapping. We have not done so here because the coupling between these mechanisms is not trivial. Residual trapping occurs along the trailing edge of the plume (i.e., the imbibition front), so we do not expect it to have a strong interaction with capillary pinning at the pinned interface or along the drainage front. Solubility trapping, however, occurs along both the imbibition front and the drainage front, and the way in which it interacts with capillary pinning is unclear.

### 7. Conclusions

We have shown via laboratory-scale experiments that capillary pinning stops the migration of immiscible gravity currents at a finite distance. In addition, capillarity at the drainage front causes the buoyant, nonwetting current to thicken, a phenomenon that we refer to here as “capillary blunting.” Using experiments in micromodels designed with pore-throat heterogeneity and anisotropy, we find that capillary pinning is caused by capillary pressure hysteresis between drainage and imbibition while capillary blunting is caused by the spatial distribution of capillary entry pressures on the drainage front. Both the length of the pinned interface and the thickness of the nose scale with the relative importance between capillarity and gravity, as described by the inverse Bond number,  $Bo^{-1}$ . Despite the strong influence of capillarity in immiscible gravity currents, the nose position of the buoyant current with respect to time follows the same scaling as that of miscible gravity currents prior to stopping, although capillarity does slow down the migration of the current.

We have developed a sharp-interface model that captures the effect of capillary pinning and blunting on the evolution of immiscible gravity currents. We apply this model to aquifers associated with actual CO<sub>2</sub> sequestration projects and find that capillary pinning and blunting could be an important mechanism in limiting the maximum extent of CO<sub>2</sub> migration, even in aquifers that are thick and permeable (i.e., low  $Bo^{-1}$ ). The reduction in maximum migration distance could reduce the risks of CO<sub>2</sub> leakage through fractures or faults present in the aquifer caprock.

### Appendix A: Numerical Implementation

We solve equation (12) for the interface height  $h$ , subject to no-flow boundary conditions at the ends of the flow domain. We approximate the step-like initial configuration of  $h = 0$  for  $x < 0$  and  $h = 1$  for  $x > 0$  with the smooth function  $h(x) = 1 - [\tanh(\beta x) + 1]/2$ , which approaches a unit step for large  $\beta$ . We solve the equation numerically using a centered finite volume method in space with forward Euler time integration [Richtmyer and Morton, 1967].

The input parameters for the model are properties of the flow cell (porosity, permeability, and dimensions), the properties of the fluids (densities and viscosities), the connate water saturation  $S_{wc}$ , the strength of capillary pressure hysteresis in the system, as quantified by  $\Delta h_c$ , and the characteristic nose height  $h_n$ .

We discretize the spatial domain into  $N$  cells of size  $dx = (x_R - x_L)/N$ , denoted with index  $i = 1, 2, \dots, N - 1, N$ .  $x_L$  and  $x_R$  are the  $x$  coordinates of the left and right boundaries of the flow domain. Integrating equation (12) over a cell,  $[x_{i-\frac{1}{2}}, x_{i+\frac{1}{2}}]$  gives the integral form of the equation for each cell  $i$ :

$$\int_{i-\frac{1}{2}}^{i+\frac{1}{2}} \left( \frac{\partial h}{\partial t} - \frac{\partial}{\partial x} \left[ \frac{(1-f)}{(1-S_{wc})} h \left( \frac{\partial h}{\partial x} + \tan \theta - \frac{\partial h_c}{\partial x} \right) \right] \right) dx = 0. \tag{A1}$$

We have a step-like initial condition such that the porous medium to the left of the initial interface is completely filled with the nonwetting fluid, and the connate water saturation in this region is assumed to be always zero (i.e.,  $S_{wc} = 0, x < 0$ ). Since we assume  $P_c$  to be the minimum drainage capillary pressure  $P_{c,min}^{dr}$  along the active drainage front where  $1 - h \geq h_n$ , we get  $\partial h_c / \partial x = 0$  for  $n_{dr} < i < n_{nose}$ , where  $n_{dr}$  is the cell closest to the pinned interface that is experiencing drainage (i.e.,  $\frac{dh_i}{dt} < 0$ ) and  $n_{nose}$  is the cell where  $1 - h < h_n$ . Similarly, since we assume  $P_c$  to be the characteristic imbibition capillary pressure on the imbibition front,  $\partial h_c / \partial x = 0$  for  $i < n_{imb}$ , where  $n_{imb}$  is the cell closest to the pinned interface that is experiencing imbibition (i.e.,  $\frac{dh_i}{dt} > 0$ ). The interface between  $n_{dr}$  and  $n_{imb}$  is pinned. On the drainage front and the imbibition front, equation (A1) reduces to

$$\int_{i-\frac{1}{2}}^{i+\frac{1}{2}} \left( \frac{\partial h}{\partial t} - \frac{\partial}{\partial x} \left[ \frac{(1-f)}{(1-S_{wc})} h \left( \frac{\partial h}{\partial x} + \tan \theta \right) \right] \right) dx = 0. \tag{A2}$$

Approximating the gravity current thickness as piecewise-constant (constant over each cell  $i$ ), we have

$$\frac{\partial h_i}{\partial t} \delta x + \{F(h)\} \Big|_{i-\frac{1}{2}}^{i+\frac{1}{2}} = 0, \tag{A3}$$

where  $F(h)$  is the flux function evaluated at the intercell edges  $(i + \frac{1}{2})$  and is given by

$$F(h) = -\frac{(1-f)}{(1-S_{wc})} h \left( \frac{\partial h}{\partial x} + \tan \theta \right). \quad (A4)$$

We use a two-point flux approximation of equation (A4),

$$F_{i+\frac{1}{2}} \approx \left\{ -\frac{(1-f)}{(1-S_{wc})} h \right\}_{i+\frac{1}{2}} \left( \frac{h_{i+1} - h_i}{\delta x} + \tan \theta \right). \quad (A5)$$

The term in the curly bracket in equation (A5) plays the role of an effective diffusion coefficient at the interface,  $D_{i+\frac{1}{2}}$ . To calculate this effective diffusion coefficient at the interface, we take the arithmetic mean of the diffusion coefficients at the adjacent grid blocks

$$D_{i+\frac{1}{2}} \approx \frac{D_i + D_{i+1}}{2}. \quad (A6)$$

Across the pinned interface, we have

$$F^+ \approx D_{dr} \left( \frac{h_{dr} - h^+}{\delta x/2} + \tan \theta \right), \quad (A7a)$$

$$F^- \approx D_{imb} \left( \frac{h^- - h_{imb}}{\delta x/2} + \tan \theta \right), \quad (A7b)$$

where  $F^+$  and  $F^-$  are the fluxes on the drainage side and the imbibition side of the pinned interface, respectively (Figure 7). For simplicity, we use  $h_{dr}$  and  $h_{imb}$  to approximate the nonlinear diffusion coefficients  $D_{dr}$  and  $D_{imb}$ . By definition, we have  $h^+ - h^- = \Delta h_c$ . Since  $h$  does not change in time along the pinned interface,  $F^+$  must equal to  $F^-$  by volume conservation. We solve for  $h^-$  by enforcing  $F^+ = F^-$

$$h^- = \frac{D_{imb} (h_{imb} - \frac{\delta x}{2} \tan \theta) + D_{dr} (h_{dr} - \Delta h_c + \frac{\delta x}{2} \tan \theta)}{D_{dr} + D_{imb}}, \quad (A8)$$

and obtain the flux across the pinned interface by substituting  $h^-$  into equation (A7).

At the nose of the current where  $1-h < h_n$ , we have  $F_{nose} = 0$  as the difference in drainage capillary pressure here is balanced by hydrostatic pressure.

To discretize the equation in time, we employ the forward Euler method, so that

$$h_i^{n+1} = h_i^n + \frac{\delta t}{\delta x} [F_{i+\frac{1}{2}} - F_{i-\frac{1}{2}}]^n. \quad (A9)$$

We update  $n_{dr}$  and  $n_{imb}$  after each time step. For drainage, a portion of the active drainage front becomes pinned when it is no longer draining (i.e.,  $\frac{dh}{dt} \geq 0$ ). For imbibition, the imbibition front starts to extend outward when the entire initial vertical interface is depinned.

### Acknowledgments

We thank Michelle Dutt for assistance with the experiments and Michael Szulczewski and Jerome Neufeld for comments. This work was partly funded by the US Department of Energy (grants DE-SC0003907 and DE-FE0002041) and the MIT/Masdar Institute Program. Additional funding was provided by the MIT Energy Fellows Program (to B.Z.), a Yale Climate and Energy Institute Postdoctoral Fellowship (to C.W.M.), a Martin Fellowship for Sustainability (to M.L.S.), the Royal Society Wolfson Research Merit Award (to H.E.H.), and the ARCO Chair in Energy Studies (to R.J.).

### References

- Barenblatt, G. I. (1952), On some unsteady motions of fluids and gases in porous medium, *Prikladnaya Mat. Mekhanika*, 16, 67–78.
- Bear, J. (1972), *Dynamics of Fluids in Porous Media*, Elsevier, N. Y.
- Bennion, D. B., and S. Bachu (2008), Drainage and imbibition relative permeability relationships for supercritical CO<sub>2</sub>/brine and H<sub>2</sub>S/brine systems in intergranular sandstone, carbonate, shale and anhydrite rocks, *Soc. Pet. Eng. J.*, 11(3), 487–496.
- Bickle, M., A. Chadwick, H. E. Huppert, M. Hallworth, and S. Lyle (2007), Modelling carbon dioxide accumulation at Sleipner: Implications for underground carbon storage, *Earth Planet. Sci. Lett.*, 255, 164–176.
- Brooks, R. H., and A. T. Corey (1966), Properties of porous media affecting fluid flow, *J. Irrig. Drain. Div. Am. Soc. Civ. Eng.*, IR2, 61–88.
- Chiaramonte, L., M. D. Zoback, J. Friedmann, and V. Stamp (2008), Seal integrity and feasibility of CO<sub>2</sub> sequestration in the Teapot Dome EOR pilot: Geomechanical site characterization, *Environ. Geol.*, 54, 1667–1675.
- Cieplak, M., and M. O. Robbins (1990), Influence of contact angle on quasistatic fluid invasion of porous media, *Phys. Rev. B*, 41(16), 11508–11521.
- Doster, F., J. M. Nordbotten, and M. A. Celia (2013), Impact of capillary hysteresis and trapping on vertically integrated models for CO<sub>2</sub> storage, *Adv. Water Resour.*, 62, 465–474.
- Dussan, E. B., and F. M. Auzerais (1993), Buoyancy-induced flow in porous media generated near a drilled oil well. Part 1. The accumulation of filtrate at a horizontal impermeable boundary, *J. Fluid Mech.*, 254, 283–311.
- Ewing, R. P., and B. Berkowitz (2001), Stochastic pore-scale growth models of DNAPL migration in porous media, *Adv. Water Resour.*, 24, 309–323.
- Frind, E. O. (1982), Seawater intrusion in continuous coastal aquifer-aquitard systems, *Adv. Water Resour.*, 5(2), 89–97.

- Garcia, R. G. (2005), Reservoir simulation of CO<sub>2</sub> sequestration and enhanced oil recovery in the Tensleep Formation, Teapot Dome field, MS thesis, Tex. A&M Univ., College Station.
- Gasda, S. E., J. M. Nordbotten, and M. A. Celia (2011), Vertically averaged approaches for CO<sub>2</sub> migration with solubility trapping, *Water Resour. Res.*, *47*, W05528, doi:10.1029/2010WR009075.
- Golding, M. J., J. A. Neufeld, M. A. Hesse, and H. E. Huppert (2011), Two-phase gravity currents in porous media, *J. Fluid Mech.*, *678*, 248–270.
- Golding, M. J., H. E. Huppert, and J. A. Neufeld (2013), The effects of capillary forces on the axisymmetric propagation of two-phase, constant-flux gravity currents in porous media, *Phys. Fluids*, *25*, 036602.
- Hesse, M. A., H. A. Tchelepi, B. J. Cantwell, and F. M. Orr, Jr. (2007), Gravity currents in horizontal porous layers: Transition from early to late self-similarity, *J. Fluid Mech.*, *577*, 363–383.
- Hesse, M. A., F. M. Orr Jr., and H. A. Tchelepi (2008), Gravity currents with residual trapping, *J. Fluid Mech.*, *611*, 35–60.
- Hortle, A., J. Xu, and T. Dance (2009), Hydrodynamic interpretation of the Waarre Fm Aquifer in the onshore Otway Basin: Implications for the CO<sub>2</sub>CRC Otway Project, *Energy Proc.*, *1*, 2895–2902.
- Huppert, H. E. (2006), Gravity currents: A personal perspective, *J. Fluid Mech.*, *554*, 299–322.
- Huppert, H. E., and A. W. Woods (1995), Gravity-driven flows in porous media, *J. Fluid Mech.*, *292*, 55–69.
- Illangasekare, T. H., J. L. Ramsey, K. H. Jensen, and M. B. Butts (1995), Experimental study of movement and distribution of dense organic contaminants in heterogeneous aquifers, *J. Contam. Hydrol.*, *20*, 1–25.
- IPCC (2005), *Special Report on Carbon Dioxide Capture and Storage*, edited by B. Metz et al., Cambridge Univ. Press, Cambridge, U. K.
- Juanes, R., E. J. Spiteri, F. M. Orr Jr., and M. J. Blunt (2006), Impact of relative permeability hysteresis on geological CO<sub>2</sub> storage, *Water Resour. Res.*, *42*, W12418, doi:10.1029/2005WR004806.
- Juanes, R., C. W. MacMinn, and M. L. Szulczewski (2010), The footprint of the CO<sub>2</sub> plume during carbon dioxide storage in saline aquifers: Storage efficiency for capillary trapping at the basin scale, *Transp. Porous Media*, *82*, 19–30.
- Krevor, S. C. M., R. Pini, L. Zuo, and S. M. Benson (2012), Relative permeability and trapping of CO<sub>2</sub> and water in sandstone rocks at reservoir conditions, *Water Resour. Res.*, *48*, W02532, doi:10.1029/2011WR010859.
- Kuuskräa, V. A., G. J. Koperna, D. Riestenberg, and R. Esposito (2009), Using reservoir architecture to maximize CO<sub>2</sub> storage capacity, *Energy Proc.*, *1*, 3063–3070.
- Lake, L. W. (1989), *Enhanced Oil Recovery*, Prentice Hall, Englewood Cliffs, N. J.
- Lee, C. H., and R. T. Cheng (1974), On seawater encroachment in coastal aquifers, *Water Resour. Res.*, *10*(5), 1039–1043.
- Lenormand, R., C. Zarcone, and A. Sarr (1983), Mechanisms of the displacement of one fluid by another in a network of capillary ducts, *J. Fluid Mech.*, *135*, 123–132.
- Lenormand, R., E. Touboul, and C. Zarcone (1988), Numerical models and experiments on immiscible displacements in porous media, *J. Fluid Mech.*, *189*, 165–187.
- Leverett, M. C. (1941), Capillary behavior of porous solids, *Trans. Am. Inst. Min. Metall. Pet. Eng.*, *142*, 152–169.
- Lindeberg, E., and D. Wessel-Berg (1997), Vertical convection in an aquifer column under a gas cap of CO<sub>2</sub>, *Energy Convers. Manage.*, *38*, S229–S234.
- MacMinn, C. W., and R. Juanes (2013), Buoyant currents arrested by convective dissolution, *Geophys. Res. Lett.*, *40*, 2017–2022, doi:10.1002/grl.50473.
- MacMinn, C. W., M. L. Szulczewski, and R. Juanes (2010), CO<sub>2</sub> migration in saline aquifers. Part 1: Capillary trapping under slope and groundwater flow, *J. Fluid Mech.*, *662*, 329–351.
- MacMinn, C. W., M. L. Szulczewski, and R. Juanes (2011), CO<sub>2</sub> migration in saline aquifers. Part 2: Capillary and solubility trapping, *J. Fluid Mech.*, *688*, 321–351.
- MacMinn, C. W., J. A. Neufeld, M. A. Hesse, and H. E. Huppert (2012), Spreading and convective dissolution of carbon dioxide in vertically confined, horizontal aquifers, *Water Resour. Res.*, *48*, W11516, doi:10.1029/2012WR012286.
- Nordbotten, J. M., and H. K. Dahle (2011), Impact of the capillary fringe in vertically integrated models for CO<sub>2</sub> storage, *Water Resour. Res.*, *47*, W02537, doi:10.1029/2009WR008958.
- Nordbotten, J. M., M. A. Celia, and S. Bachu (2006), Similarity solutions for fluid injection into confined aquifers, *J. Fluid Mech.*, *561*, 307–327.
- Pennell, K. D., G. A. Pope, and L. M. Abriola (1996), Influence of viscous and buoyancy forces on the mobilization of residual tetrachloroethylene during surfactant flushing, *Environ. Sci. Technol.*, *30*(4), 1328–1335.
- Riaz, A., M. Hesse, H. A. Tchelepi, and F. M. Orr Jr. (2006), Onset of convection in a gravitationally unstable, diffusive boundary layer in porous media, *J. Fluid Mech.*, *548*, 87–111.
- Richtmyer, R. D., and K. W. Morton (1967), *Difference Methods for Initial Value Problems*, John Wiley, Chichester, U. K.
- Szulczewski, M. L., C. W. MacMinn, H. J. Herzog, and R. Juanes (2012), Lifetime of carbon capture and storage as a climate-change mitigation technology, *Proc. Natl. Acad. Sci. U. S. A.*, *109*(14), 5185–5189.
- Underschultz, J., C. Boreham, T. Dance, L. Stalker, B. Freifeld, D. Kirste, and J. Ennis-King (2011), CO<sub>2</sub> storage in a depleted gas field: An overview of the CO<sub>2</sub>CRC Otway Project and initial results, *Int. J. Greenhouse Gas Control*, *5*, 922–932.
- van Genuchten, M. T. (1980), A closed-form equation for predicting the hydraulic conductivity of unsaturated soils, *Soil Sci. Soc. Am. J.*, *44*, 892–898.
- Weir, G. J., S. P. White, and W. M. Kissling (1996), Reservoir storage and containment of greenhouse gases, *Transp. Porous Media*, *23*(1), 37–60.
- Wilkinson, D., and J. Willemsen (1983), Invasion percolation: A new form of percolation theory, *J. Phys. A Math. Gen.*, *16*, 3365–3376.
- Yortsos, Y. C. (1995), A theoretical analysis of vertical flow equilibrium, *Transp. Porous Media*, *18*, 107–129.
- Zhao, B., C. W. MacMinn, M. L. Szulczewski, J. A. Neufeld, H. E. Huppert, and R. Juanes (2013), Interface pinning of immiscible gravity-exchange flows in porous media, *Phys. Rev. E*, *87*, 023015.
- Zhou, D., F. J. Fayers, and F. O. Jr. (1997), Scaling of multiphase flow in simple heterogeneous porous media, *Soc. Pet. Eng. J.*, *12*(3), 173–178.